Research Square

Preprints are preliminary reports that have not undergone peer review.
They should not be considered conclusive, used to inform clinical practice,
or referenced by the media as validated information.

Metabolic heterogeneity and phenotypic switches in the tumor microenvironment identified using a modular modeling approach

Andrey Naumenya

ups_ups_ups@list.ru

Sirius University of Science and Technology

Ilya Akberdin

Sirius University of Science and Technology

Article

Keywords:

Posted Date: November 17th, 2026

DOI: https://doi.org/10.21203/rs.3.rs-11758017/v1

License: This work is licensed under a Creative Commons Attribution 4.0 International License.
Read Full License

Additional Declarations: No competing interests reported.

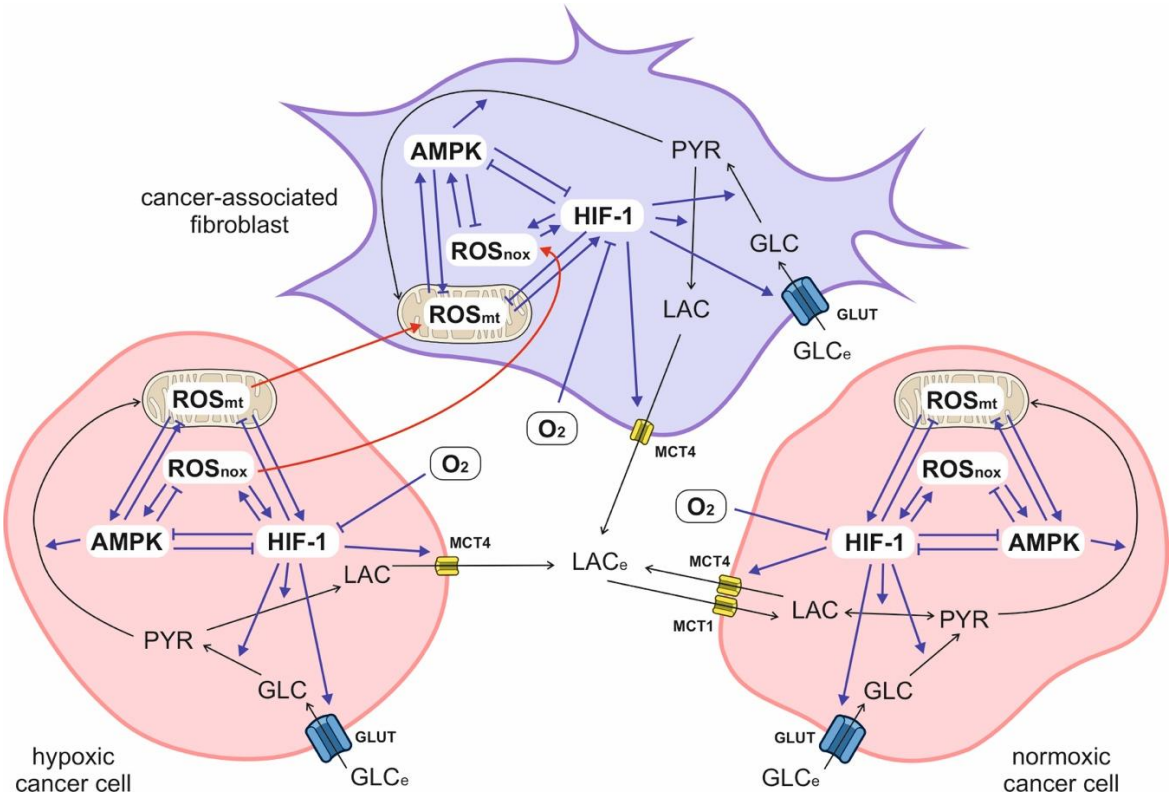
Metabolic heterogeneity and phenotypic switches in the tumor microenvironment identified using a modular modeling approach

Andrey S. Naumenya[1*], Ilya R. Akberdin[1]

[1]*Sirius University of Science and Technology, Olympic Ave., 1, Sirius Federal Territory, Krasnodar region, Russia, 354340*

[*]*Corresponding author: Andrey S. Naumenya, ups_ups_ups@list.ru*

Abstract



Metabolic heterogeneity and plasticity of malignant tumors, regulated by the HIF-1/AMPK/ROS signaling network, are defining hallmarks of cancer, which requires the use of single-cell technologies for its experimental study and significantly limits the effectiveness of drugs. Mathematical modeling has demonstrated fundamental and practical significance in this aspect of the cancer research. However, existing kinetic models describe only individual features of the cellular metabolism or regulation. To address this gap, we developed a modular mechanistic model implemented on the BioUML platform that integrates central carbon metabolism with regulatory signaling to simulate interacting cancer cells

and cancer-associated fibroblasts. The model captures the reverse Warburg effect: a hypoxic cancer cell reprograms a neighboring fibroblast into a glycolytic phenotype via ROS signaling, and the lactate secreted by the fibroblast is subsequently consumed by a normoxic cancer cell. Parametric analysis reveals that under glucose limitation, this reverse Warburg phenotype is energetically more favorable for cancer cells than the classical Warburg phenotype. These results provide a quantitative foundation for understanding complex intercellular interactions within tumors and offer testable predictions for experimental validation.

Synopsis

A kinetic model integrating central carbon metabolism with HIF-1 and AMPK signaling provides a quantitative foundation for understanding tumor metabolic heterogeneity. By simulating intercellular crosstalk, the modular approach elucidates the mechanistic basis and bioenergetic consequences of the reverse Warburg effect.

- A modular kinetic model is developed that integrates central carbon metabolism with the HIF-1–AMPK–ROS regulatory circuit and deciphers how intercellular interactions drive phenotype switching.
- The model reproduces the reverse Warburg effect, predicting that fibroblast reprogramming occurs over a timescale of weeks, consistent with experimental observations.
- Quantitative analysis of the constructed model predicts that the reverse Warburg phenotype provides a bioenergetic advantage over the classical Warburg phenotype under glucose limitation, provided that extracellular lactate remains available.

Introduction

Despite significant progress in cancer therapy, the mortality rate remains alarmingly high [1]. The limited effectiveness of current treatments stems largely from the extraordinary diversity of malignant cell populations and their innate capacity for metabolic adaptation. Because of this heterogeneity, distinct phenotypic subpopulations coexist within a single tumor [2]. Each subpopulation maintains a specific bioenergetic state that enables survival under particular microenvironmental conditions — for instance, low oxygen tension, restricted nutrient availability, or specific intercellular signals. These states are dynamic and are continuously remodeled in response to local changes [3]. The metabolic flexibility, and in particular the ability to switch between phenotypes, is a major contributor to disease progression and the development of therapeutic resistance [4,5].

A central feature of this flexibility is the ability of cancer cells to switch between distinct metabolic phenotypes, the most prominent being the Warburg effect. First described by Otto Warburg in the 1920s [6], this phenomenon refers to the preference of tumor cells for glycolysis even under normoxic conditions — a strategy known as aerobic glycolysis. This metabolic reprogramming may seem paradoxical, since glycolysis yields far less ATP per glucose molecule than oxidative phosphorylation. However, aerobic glycolysis provides several crucial advantages for rapidly dividing cells: it produces ATP at a faster rate, supplies glycolytic intermediates that support biosynthesis and cell growth, and generates lactate that acidifies the microenvironment, thereby promoting invasion and suppressing antitumor immune responses [7]. An alternative to this glycolytic phenotype — often termed the reverse Warburg effect — is observed when normoxic cancer cells consume and oxidatively metabolize lactate that is produced and secreted by reprogrammed stromal fibroblasts [8,9]. Under the influence of signals such as reactive oxygen species (ROS) and transforming growth factor β (TGF-β), fibroblasts adopt a glycolytic phenotype and become net exporters of lactate, which cancer cells then use as an oxidative substrate [10,11]. A related but distinct form of metabolic cooperation, the lactate shuttle, occurs when normoxic cancer

cells import and metabolize lactate released by neighboring hypoxic cancer cells. This coupling allows the tumor to recycle lactate and sustain oxidative ATP production in oxygenated regions without consuming glucose [12]. A number of signaling pathways have been implicated in the control of metabolic phenotype, yet how these pathways are coordinated to execute the switch remains incompletely understood.

Key nodes in this regulatory network include hypoxia-inducible factor 1 (HIF-1) and AMP-activated protein kinase (AMPK), whose mutual regulation is thought to play a central role in metabolic switching [13]. HIF-1 drives the expression of glycolytic enzymes and glucose transporters, thereby promoting biosynthesis and contributing to redox balance. Beyond its role in glycolysis, HIF-1 regulates angiogenesis, cell survival, and metabolic reprogramming. In contrast, AMPK acts as both a cellular energy sensor and a tumor-suppressive kinase: it is activated under energetic stress, promotes mitochondrial respiration, and inhibits anabolic processes. HIF-1 and AMPK engage in reciprocal regulation: AMPK suppresses HIF-1 activity, whereas HIF-1 downregulates AMPK expression, forming a feedback loop that enables metabolic switching [14–16].

Additionally, mitochondria and the ROS they generate are integral to this regulatory network [17]. Although Warburg originally linked aerobic glycolysis to mitochondrial dysfunction, many cancer cells retain functional mitochondria [18]. These organelles nevertheless contribute substantially to the cellular ROS pool, which in turn modulates AMPK and HIF-1 activity, thereby shaping the metabolic phenotype [19]. The resulting network — interlocking HIF-1, AMPK, and ROS across heterogeneous cell populations — forms a system of intertwined feedback loops whose integrated behavior is difficult to resolve from experimental snapshots alone.

Mathematical modeling offers a complementary strategy: it integrates available data into a consistent framework and, once calibrated, provides a systematic exploration of parameter space to uncover mechanisms that are difficult or impossible to measure directly. Reflecting this potential, several computational models have already addressed aspects of cancer metabolism and its regulation [20–24]. However, they cover only fragments of the phenotype switching problem. Mosca and coauthors [21] constructed a kinetic model of glucose metabolism with simplified HIF-1-mediated regulation and, using sensitivity analysis, identified specific glycolytic enzymes that exert the greatest influence on metabolic flux as potential therapeutic targets. Yu et al. [23] developed a regulatory circuit model of HIF-1, AMPK and ROS, demonstrating distinct metabolic states and simulating therapeutic interventions. Building on this regulatory framework, Jia and coauthors [24] coupled the HIF-1–AMPK–ROS circuit to the metabolic pathways of glucose oxidation, glycolysis and fatty acid oxidation, and showed that cancer cells can stably reside in a hybrid metabolic state. Aghakhani et al. [20] built a hybrid model combining Boolean regulation with flux balance analysis, reproducing the reverse Warburg effect in breast cancer-associated fibroblasts and identifying HIF-1 as its driver. Shan and coauthors [22] employed an agent-based model to show that the reverse Warburg effect slows growth in favorable microenvironments but confers an advantage under resource limitation. Despite these contributions, no kinetic models currently describe a phenotype switching in individual cells and account for metabolic interactions between different cell populations within the tumor microenvironment.

To address this gap, we propose a modular framework that integrates the kinetic models describing metabolism (Fig. 1A) and signaling in tumor cells [21,23] and extends them to describe multiple cells (Fig. 1B). This framework enables us to systematically investigate how the interplay between metabolism and signaling drives phenotype switching in single cells and in interacting cell populations. This framework allows us to investigate metabolic interactions between cancer cells and

with the surrounding stroma, providing a quantitative basis for understanding how ROS and intercellular communication shape tumor heterogeneity and plasticity.

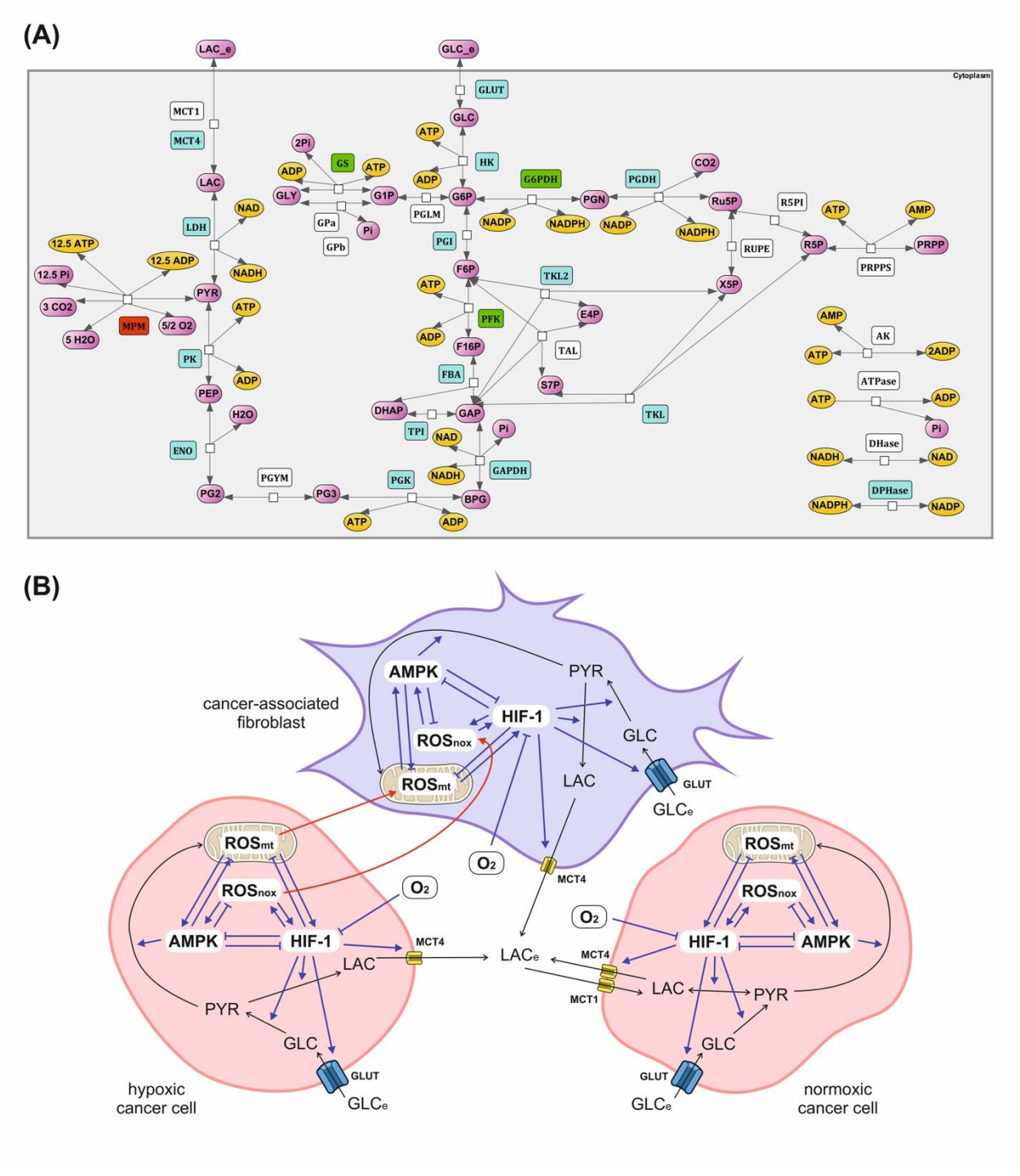


Figure 1. Modular architecture and intercellular interactions of the model. *(A) Metabolic module (adapted and redrawn from Mosca et al. [21]) describing central carbon metabolism; metabolites are shown in pink, cofactors in yellow, and enzyme regulation is color-coded: white – no*

regulation, cyan – HIF-1 only, red – AMPK only, green – both HIF-1 and AMPK.

(B) A scheme of the three-cell model, comprising two cancer cells and a cancer-associated fibroblast. The cells communicate via a shared extracellular lactate pool and ROS-mediated signaling; for each cell, the complete regulatory network [23] is represented by the white boxes. Black arcs designate biochemical conversion, while blue arcs and blunt-tipped arrows correspond to activation and repression processes respectively. Red arcs denote intercellular ROS signaling from the hypoxic cancer cell to the fibroblast.

Materials and Methods

Model development platform

The model was implemented using the BioUML platform, an integrated environment for modular and visual modeling of complex biological systems. BioUML supports major systems biology standards, including SBML and SBGN, and allows a model to be constructed as a hierarchical diagram from which simulation-ready code is generated automatically [25–28]. A critical feature for the particular study is its native support for modular composition: individual submodels can be encapsulated as modules with clearly defined interfaces and connected without modifying their internal equations. We used this capability to combine six sub-diagrams — the regulatory and metabolic modules of each of the three cells — into a single composite framework, which provides a shared extracellular lactate pool and enables ROS-mediated intercellular signaling. The platform automatically resolves all inter-module connections via import, output and connection ports and flattens the composite model into a self-consistent system of ordinary differential equations [29–32]. BioUML is integrated with Jupyter Notebook, providing an interactive environment for parameter exploration, in-line

visualization, and reproducible research. The Jupyter Notebooks with detailed stages of the model simulations are available in the Data Availability.

Regulatory module

The regulatory network was adapted from Yu and coauthors' model [23], which describes the core circuit of HIF-1, AMPK, and ROS. This model captures the mutual inhibition between HIF-1 and AMPK, the regulation of ROS production by both factors, and the feedback loops that determine the metabolic phenotype. The original model defines three stable states for cancer cells — glycolytic (W), oxidative (O), and hybrid (W/O) — and two states for normal cells (O and W), with the distinction encoded in parameter values governing ROS production and HIF-1 degradation. We used the original equations without modification, except that we retained the oxygen-dependent HIF-1 degradation term to model hypoxic conditions, whereas Yu and coauthors introduced it to simulate hyperbaric oxygen therapy.

Metabolic module

The metabolic network was adapted from the *in silico* study of Mosca and coauthors [21], which describes central carbon metabolism including glycolysis, the pentose phosphate pathway (PPP), glycogen synthesis and degradation (GS), and mitochondrial pyruvate metabolism (MPM). Mitochondrial processes are originally described schematically by a single reaction. To enable simulation of the phenotype switching and intercellular interactions, we introduced several modifications.

First, we added equations describing lactate transport via monocarboxylate transporters (MCT1 and MCT4) and lactate degradation. The net lactate flux is the difference between export via MCT4 and import via MCT1:

$$J_{MCT} = \text{HIF_regulation} \cdot V_{max}^{MCT4} \cdot \frac{[LAC]}{K_m^{MCT4} + [LAC]} - V_{max}^{MCT1} \cdot \frac{[LAC_e]}{K_m^{MCT1} + [LAC_e]}$$

Here, HIF-1-dependent regulation is applied only to the exporter MCT4; the importer MCT1 is treated as HIF-1-independent, based on the experimental findings of Ullah and coauthors [33]. The positive regulation of MCT4 by HIF-1 is:

$$\frac{1 + \beta_{HIF_MCT} \left(\frac{HIF1}{HIF_0}\right)^n}{1 + \left(\frac{HIF1}{HIF_0}\right)^n}$$

The net MCT flux directly enters the mass balance for intracellular lactate. Lactate degradation was modeled as a first-order process: $J_{LAC_deg} = k_{d_LAC} \cdot [LAC_e]$.

Second, we modified the MPM equation to provide flexible control of the energetic state, because the original formulation produced non-physiological pyruvate concentrations, which dropped below 10^{-12} M or even reached negative values under certain simulation parameters. The modified equation follows Michaelis-Menten kinetics with respect to pyruvate, multiplied by an AMPK-dependent regulation term and an ATP-inhibited term:

$$J_{MPM} = \text{AMPK_regulation} \cdot V_{max}^{MPM} \cdot \frac{[PYR]}{K_m^{MPM} + [PYR]} \cdot \frac{1}{1 + \frac{[ATP]}{K_{ATP}}}$$

The positive regulation of MPM by AMPK follows the same general Hill-type equation as for the other enzymes, which is described below.

Third, we extended the regulatory layer of the metabolic module. Whereas the original Mosca model [21] included only HIF-1-mediated regulation, we introduced additional AMPK-dependent regulation for several key enzymes. All regulatory

effects are implemented as multiplicative Hill-type factors acting on V_{max}. For positive regulation by HIF-1:

$$\frac{1 + \beta_{HIF}\left(\frac{HIF1}{HIF_0}\right)^n}{1 + \left(\frac{HIF1}{HIF_0}\right)^n}$$

For positive regulation by AMPK:

$$\frac{1 + \beta_{AMPK}\left(\frac{AMPK}{AMPK_0}\right)^n}{1 + \left(\frac{AMPK}{AMPK_0}\right)^n}$$

For negative regulation by AMPK:

$$\frac{1 + \frac{1}{\beta_{AMPK}}\left(\frac{AMPK}{AMPK_0}\right)^n}{1 + \left(\frac{AMPK}{AMPK_0}\right)^n}$$

For all regulated enzymes, β_{HIF} and β_{AMPK} were set to 20, and the Hill coefficient n was set to 3. The complete list of regulated enzymes is provided in Supplementary Table S1.

Coupled model

The regulatory and metabolic modules were coupled by transmitting HIF-1 and AMPK concentrations with a time delay comprising a typical time frame for transcription and translation processes. We assume a single, uniform delay of 12 h for all enzymes, implemented via the built-in delay function of BioUML. This value, although not precisely known, can be refined when experimental data become available.

When integrating the Mosca and Yu models [21,23], we encountered a mismatch in the time axis scales: the intrinsic times of the two models differ and must be aligned to obtain physiologically meaningful switching dynamics. To resolve this, we introduced a normalization coefficient of 6.0×10^{-4}, meaning that one hour of real time corresponds to 6.0×10^{-4} units of the simulation time in the Mosca's metabolic module. For the regulatory module of Yu et al., all reaction rates were multiplied by a factor of 1666.667, together with an analogous time correction, to bring its dynamics onto the same time scale.

Intercellular interactions

Cells interact via shared extracellular pools. In all multicellular configurations, the concentration of extracellular lactate, $[LAC_e]$, is governed by the net MCT fluxes from each cell and a first-order degradation term:

$$\frac{d[LAC_e]}{dt} = \sum_{cells} \left(J_{MCT4}^{export} - J_{MCT1}^{import} \right) - k_{d_LAC} \cdot [LAC_e]$$

In the three-cell configuration, where the reverse Warburg effect is driven by a hypoxic cancer cell, the fibroblast senses a weighted mixture of its own intracellular ROS and the ROS originating from the hypoxic cancer cell, with a time delay representing intercellular signaling:

$$ROS_{total}(t) = (1-\rho) \cdot \left([ROS_{mt}(t)] + [ROS_{nox}(t)] \right) + \rho \cdot \left(\left[ROS_{hyp_mt}(t-\tau) \right] + \left[ROS_{hyp_nox}(t-\tau) \right] \right)$$

This ROS_{total} directly replaces the fibroblast's own ROS in the regulatory module. The parameters were set to $\rho = 0.5$ and $\tau = 1$ h.

Hypoxia can be applied independently to individual cells. For normoxic cells the oxygen concentration is 6.5×10^{-5} M [21]; under hypoxia this value is decreased by a factor of 10 [34]. The corresponding changes in other parameters are described in the Results.

Model configurations overview

We consider the model evolution in three stages of increasing complexity, differing in the number of simulated cells and the corresponding intercellular interactions. The single-cell configuration comprises one cancer cell and is used to study intrinsic phenotype switching between the oxidative, glycolytic, and hybrid states. The two-cell configuration introduces a second cancer cell, so that two cancer cells communicate via a shared extracellular lactate pool; this allows investigation of the lactate shuttle between hypoxic and normoxic cancer cells. The three-cell configuration adds a cancer-associated fibroblast and incorporates ROS-mediated intercellular signaling, reproducing the reverse Warburg effect driven by a hypoxic cancer cell. This stepwise increase in complexity enables the intrinsic phenotypic plasticity of individual cells to be decoupled from the effects of intercellular metabolic coupling.

Definition of metabolic phenotypes

Cellular phenotypes are defined in the model framework at two levels: regulatory and metabolic. At the regulatory level, the state is determined by the steady-state concentrations of HIF-1 and AMPK. We distinguish three states: the glycolytic (W) phenotype, marked by high HIF-1 and low AMPK; the oxidative (O) phenotype, characterized by low HIF-1 and high AMPK; and the hybrid (W/O) phenotype, in which both regulators are elevated. These three regulatory states correspond to those originally defined by Yu and coauthors [23]. At the metabolic level, phenotypes are defined by the direction and magnitude of two key fluxes: the LDH flux as a marker of glycolysis, and MPM as a marker of oxidative phosphorylation. In the W phenotype, the LDH flux is directed towards lactate production, and MPM is low.

The W/O phenotype features simultaneous glycolytic and oxidative activities, whereas the LDH flux is near zero and MPM is high for the O phenotype. The reverse Warburg (RW) phenotype is a distinct subtype of the O state in which the LDH reaction is reversed, actively consuming extracellular lactate, and the cell relies predominantly on oxidative metabolism of imported lactate. This state is observed in normoxic cells that have been metabolically coupled to glycolytic neighbors and reflects a stable, rather than transient, metabolic adaptation.

Model simulations: settings, model parameters and initial values

All simulations followed a common protocol. Each cell was initialized under normoxia and started in the O phenotype. Hypoxia was applied exactly 168 h after the simulation start; this time point is marked by a dashed vertical line on all temporal plots. The duration of hypoxia varied depending on the specific experiment, and the exact value used in each case is provided in the corresponding Jupyter Notebooks.

All parameters, except those listed in Table 1, were taken from the original models of Mosca et al. [21] and Yu et al. [23]. To obtain the initial values, we used the three-cell configuration simulated without hypoxia; the resulting steady-state concentrations are presented in Table 2.

Parameter	Description	Value
Metabolic enzymes		
Katp_MPM	ATP inhibition constant for mitochondrial pyruvate metabolism (MPM) [21]	0.0087 M
Km_MPM	Michaelis constant for MPM [35]	1.50×10^{-4} M
Km_MCT1	Michaelis constant for MCT1-mediated lactate transport [36]	0.0035 M
Km_MCT4	Michaelis constant for MCT4-mediated lactate transport [36]	0.028 M
Vmax_MCT1	Maximum flux of MCT1	75 nmol/min/mg

Vmax_MCT4	Maximum flux of MCT4	150 nmol/min/mg
Vmax_MPM	Maximum flux of MPM	80 nmol/min/mg
k_d_LAC	Degradation rate constant of extracellular lactate (single-cell configuration)	0.48 h^{-1}
k_d_LAC	Degradation rate constant of extracellular lactate (two-cell configuration)	0.96 h^{-1}
k_d_LAC	Degradation rate constant of extracellular lactate (three-cell configuration)	1.44 h^{-1}
Regulatory parameters		
β_HIF	Strength factor of HIF-mediated enzyme regulation	20
β_AMPK	Strength factor of AMPK-mediated enzyme regulation	20
n	Hill coefficient for enzyme regulation	3
β_HIF_MCT	Strength factor of HIF-mediated MCT4 regulation	3
HIF0_c	Normalization value for HIF in enzyme regulation in cancer cells	295.1 nM
AMPK0_c	Normalization value for AMPK in enzyme regulation in cancer cells	327.4 nM
HIF0_f	Normalization value for HIF in enzyme regulation in fibroblasts	290 nM
AMPK0_f	Normalization value for AMPK in enzyme regulation in fibroblasts	150 nM

Table 1. Parameters introduced or modified in the present work. *Only those parameters that were added or changed relative to the original models of Mosca et al.* [21] *and Yu et al.* [23] *are listed. All other parameters were used as published and are not reproduced here. The table is divided into two sections: metabolic enzymes and regulatory parameters. For the parameter k_d_LAC, which depends on the number of simulated cells, the relevant configuration is specified in the Description column, and the corresponding numerical value is given in the Value column.*

	Cancer cells	Fibroblast	
GLC	6.410E-04	8.316E-04	M
G6P	4.181E-04	5.183E-04	M
ADP	7.491E-03	7.901E-03	M
ATP	3.909E-03	3.499E-03	M
F6P	2.300E-05	2.862E-05	M
F16P	3.579E-04	2.511E-04	M
E4P	2.429E-07	2.347E-07	M
PGN	1.690E-07	7.843E-07	M
NADP	1.570E-06	7.228E-07	M
NADPH	1.775E-05	1.860E-05	M
BPG	3.237E-05	2.867E-05	M
RU5P	1.779E-07	2.622E-07	M
X5P	5.129E-07	7.508E-07	M
R5P	1.640E-07	2.314E-07	M
GAP	1.260E-04	1.100E-04	M
S7P	1.347E-08	1.892E-08	M
NADH	4.831E-06	4.793E-06	M
NAD	1.340E-03	1.340E-03	M
AMP	3.110E-03	3.110E-03	M
PRPP	1.000E-03	1.000E-03	M
G1P	2.687E-05	3.321E-05	M
Pi	2.000E-02	2.000E-02	M
GLY	2.084E-01	2.084E-01	M
CIT	1.080E-03	1.080E-03	M
F26P	3.670E-06	3.670E-06	M
DHAP	5.471E-04	4.879E-04	M
PG3	2.639E-05	2.130E-05	M
PG2	3.805E-05	3.025E-05	M
PEP	3.702E-05	2.912E-05	M
PYR	6.403E-05	7.721E-05	M
LAC	7.460E-04	7.827E-04	M
CO2	2.140E-02	2.140E-02	M
O2	6.500E-05	4.520E-05	M
LAC_e	9.139E-05		M
GLC_e	1.000E-02		M
HIF-1	26.78	34.93	nM
AMPK	437.3	338.1	nM
ROS_mt	128.8	55.64	μM

ROS_nox	2.319	2.772	μM

Table 2. Initial values of state variables. *Concentrations used to initialize the simulations, given separately for cancer cells and fibroblasts. Extracellular species (LAC_e, GLC_e) are distinguished from intracellular metabolites. Values were obtained from a simulation of the three-cell configuration run without hypoxia.*

Results and Discussion

Reconstruction of the modular model

The regulatory core of our framework is the HIF-1–AMPK–ROS circuit described by Yu and coauthors [23], which serves as the decision-making layer. This model captures the mutual inhibition of HIF-1 and AMPK and the dual regulation of ROS production, and it predicts three stable steady states (O, W/O, W) for cancer cells and two (O, W) for fibroblasts. The metabolic layer is built upon the kinetic model of Mosca and coauthors [21], which provides a description of glycolysis, the pentose phosphate pathway, glycogen turnover, and mitochondrial pyruvate metabolism. Together, these two modular components cover the signaling and metabolic levels required to describe the phenotype switch.

To enable intercellular communication, we extended the Mosca model with lactate transport via MCT1 and MCT4. MCT4 is placed under HIF-1-dependent regulation, while MCT1 is treated as constitutive [33]. A first-order lactate degradation process was added to represent washout by the circulation or consumption by other cell types. We also replaced the original schematic HIF-1-mediated regulation with detailed Hill-type equations and introduced AMPK-dependent regulation for several key enzymes, so that the metabolic response faithfully reflects the regulatory state. The MPM equation was reformulated to enable flexible tuning of oxidative flux and avoid the

non-physiological pyruvate concentrations produced by the original formulation under conditions far from the W/O state.

Several assumptions were introduced during the model construction. All enzymes share a single transcriptional–translational delay of 12 h [37,38], implemented via the built-in delay function of BioUML. The Hill-type regulatory factors use identical parameters for all regulated enzymes, whereas in reality enzyme sensitivities to HIF-1 and AMPK are known to differ [39], but direct experimental measurements are unavailable for considered enzymes. Furthermore, intercellular ROS signaling is simplified: we assume that a fraction of the fibroblast's intrinsic ROS is substituted by ROS from the hypoxic cancer cell, applied with a time delay.

The result of these extensions is a composite model that encompasses the regulatory logic, metabolic fluxes, and intercellular exchange necessary to study phenotypic switching. The modular model is available via GitLab repository: https://gitlab.sirius-web.org/AndreyNaumenya/reverse-warburg-effect.

Single-cell phenotypes

We compared the steady-state fluxes and metabolite concentrations characteristic of the O, W, and W/O phenotypes (Supplementary Tables S2, S3). Glycolysis is suppressed in the O cellular phenotype: glucose consumption is low, the pentose phosphate pathway (PPP) accounts for ~6% of the consumed glucose, more than 80% of the carbon flux enters the mitochondria, and less than 10% of glucose is converted to lactate; intracellular ATP remains at approximately 3.5 mM [40]. The W phenotype elevates the glucose uptake roughly 8-fold relative to normoxia under sustained hypoxia. The PPP share is approximately 20%, whereas mitochondrial oxidation drops to ~3% of carbon flux, and ~85% of glucose is excreted as lactate [41]. ATP levels keep low despite the high glycolytic rate, illustrating the inefficiency of the Warburg strategy. The flux distribution in the W/O hybrid phenotype is

broadly consistent with that reported by Mosca and coauthors [21]. Notably, the ATP concentration in W/O cells is several-fold higher than in either the O or the W phenotype, confirming the bioenergetic advantage of the hybrid state under fluctuating oxygen availability.

Regulatory changes precede metabolic ones by a time delay corresponding to transcription and translation. Throughout the text, when a cell is described as being in a certain phenotype, both regulatory and metabolic criteria are implied unless otherwise stated.

Switching in the single-cell configuration

According to simulations, hypoxic exposure exceeding 22 h followed by reoxygenation drives the cell into the hybrid W/O state; at least 4 days of continuous hypoxia is required for a complete glycolytic W transition (Fig. 2A, B). These threshold values follow directly from the parameter set inherited from the Yu and coauthor's model. They should therefore be viewed as a consequence of that regulatory circuit rather than as experimentally measured parameters. However, these timescales are physiologically realistic [42]. The existence of a sharp transition is robust, while the exact times may shift with parameter choices.

Figure 2C displays a hysteresis plot for HIF-1 and AMPK. To construct this plot, we fixed one variable at a series of values and, for each fixed value, computed the steady-state concentration of the second variable. The procedure was then repeated with the roles of the two variables reversed. The three intersections of the forward and reverse curves correspond to the three stable steady states O, W/O, and W of the cancer cell, confirming its tristable behavior. The corresponding hysteresis plot for the HIF-1 and AMPK pair in the fibroblast is provided in Supplementary Fig. S1.

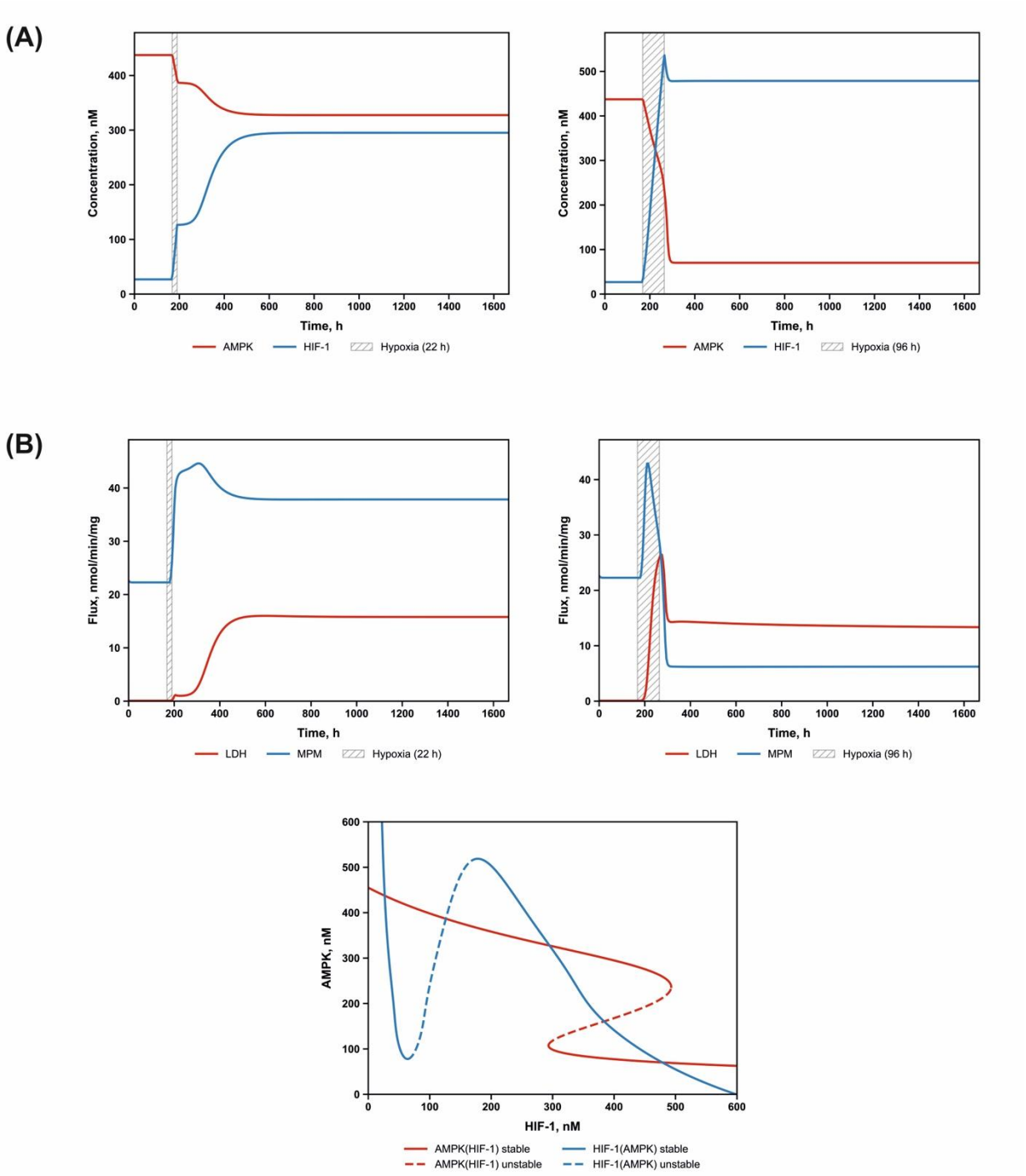


Figure 2. Single-cell switching dynamics. *(A) Time courses of HIF-1 and AMPK during hypoxia of varying duration. The period of hypoxic exposure is delimited by dashed vertical lines.*

(B) Corresponding LDH and MPM fluxes. The hypoxic interval is marked as in panel A. At the moment of switching, a transient flux overshoot is observed, which subsequently settles to a plateau. The steady-state LDH flux in the W phenotype is marginally lower than that in the W/O phenotype.

(C) Hysteresis plot for HIF-1 versus AMPK. The three intersection points of the forward and reverse branches correspond to the O, W/O, and W steady states seen in panel A, confirming the tristable behavior of the cancer cell [23].

Multi-cell interactions

Two-cell configuration

To examine metabolic coupling between two cancer cells, we subjected one cell to hypoxia while leaving the second cell in normoxia. The hypoxic cell autonomously switches to a glycolytic phenotype (W or W/O, depending on the duration of hypoxia) and exports lactate into the shared extracellular space. The normoxic cell, sensing the elevated extracellular lactate, imports it via MCT1 and shifts towards the RW phenotype. Because this two-cell system does not involve stromal cells, the observed metabolite exchange corresponds specifically to a lactate shuttle between cancer cells rather than to the canonical reverse Warburg effect, which requires fibroblast participation.

The rate of lactate consumption by the normoxic cell is largely insensitive to whether the hypoxic cell resides in the W or the W/O state, since both phenotypes generate comparable extracellular lactate levels. The extracellular lactate concentration is governed by the balance between net export from the hypoxic cell and a first-order degradation process with rate constant k_{d_LAC}. The degradation represents washout by the circulation or consumption by other cell types not explicitly represented in the model. The value of k_{d_LAC} can be adjusted to bring the steady-state extracellular lactate concentration into the physiologically relevant range (0.5–20 mM) [43]. At the default value used here, the steady-state concentration is within this interval, ensuring that the subsequent analysis is performed under physiologically meaningful conditions.

Three-cell configuration

To investigate whether a glycolytic cancer cell can reprogram a neighboring fibroblast, we simulated a system comprising two cancer cells and one fibroblast that share a common extracellular lactate pool. In this configuration, the normoxic cancer cell is able to import lactate via MCT1, as illustrated by the time course of lactate uptake in Figure 3A.

All cells initially reside in the O phenotype according to the model settings. One cancer cell is then subjected to hypoxia, whereupon it autonomously transitions to the W phenotype. As a consequence of this transition, its intracellular ROS level drops, a behavior inherent to the original[23] regulatory circuit (Supplementary Fig. S2). The fibroblast is coupled to the hypoxic cancer cell through direct ROS exchange controlled by the parameter ρ, which represents the fraction of the fibroblast's total ROS that is replaced by the ROS originating from the hypoxic cancer cell. When $\rho = 0.5$, the fibroblast senses a marked reduction in ROS and, following the regulatory logic of the Yu et al. model [23], undergoes a switch from O to W. The temporal profiles of HIF-1 and AMPK in the fibroblast during this reprogramming are shown in Figure 3B, and the predicted switching time falls within the 2–3 week range observed experimentally [44]. The hypoxic cancer cell thus imposes a glycolytic phenotype on the fibroblast — the hallmark of the reverse Warburg effect.

The switching behavior depends critically on ρ, which reflects the spatial proximity between the two cells and the strength of the paracrine signal. For $\rho < 0.45$, the fibroblast remains in the O state. Once ρ exceeds this threshold, fibroblast switching becomes possible, and the time required to complete the transition decreases as ρ increases (Figure 3C). At $\rho = 1$, the fibroblast reaches the W phenotype within approximately 12 days. These results indicate that the reverse Warburg effect is spatially constrained: only fibroblasts located within a critical distance from a glycolytic cancer cell can be metabolically reprogrammed.

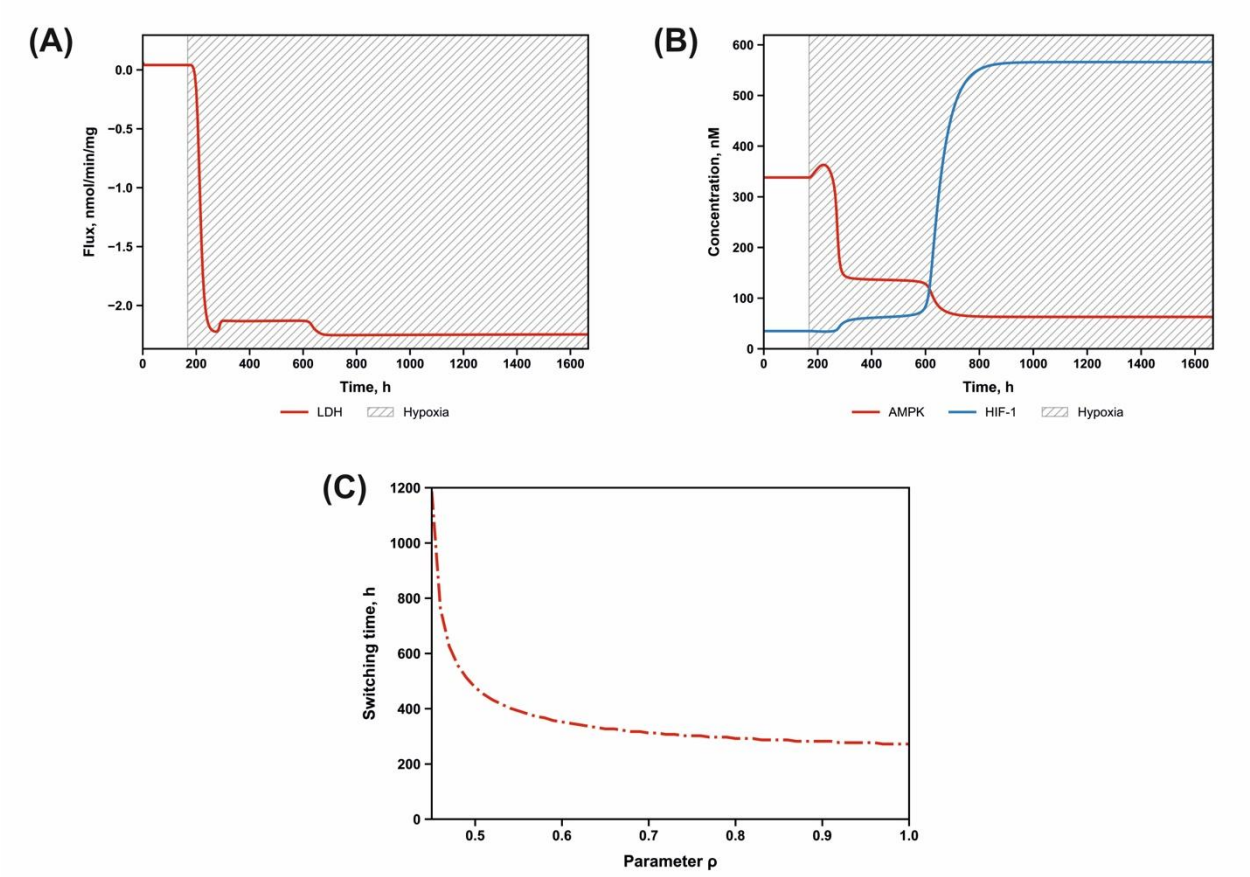


Figure 3. Fibroblast reprogramming in the three-cell configuration. *(A) Time course of lactate uptake by the normoxic cancer cell, reflected by a negative LDH flux. Under glucose-replete conditions, fibroblast switching does not substantially alter the rate of lactate consumption. (B) Temporal profiles of HIF-1 and AMPK in the fibroblast during reprogramming ($\rho = 0.5$). The AMPK level declines almost immediately. HIF-1 rises only after a delay and dictates the overall switching time. (C) Dependence of the fibroblast switching time on the coupling parameter ρ. At $\rho = 0.45$, switching is extremely slow. At $\rho = 1$, the fibroblast reaches the W phenotype within approximately 12 days.*

Parametric analysis

Regulation parameters.

We systematically analyzed how the key regulatory parameters affect the metabolic phenotype. The coefficients β_{HIF} and β_{AMPK} determine the strength of enzyme

expression regulation by HIF-1 and AMPK, respectively, and the Hill coefficient n determines the cooperativity of binding and the resulting nonlinearity of the regulatory response. In cancer-associated fibroblasts (CAFs), both β_{HIF} and β_{AMPK} strongly influence the W phenotype: the magnitude of lactate production varies substantially with both parameters (Supplementary Fig. S3). In normoxic cancer cells, by contrast, the appearance of the RW phenotype was largely insensitive to β_{AMPK}. We varied both β_{HIF} and β_{AMPK} and observed that the LDH flux remained negative over a wide range of β_{AMPK} values, provided that β_{HIF} exceeded a certain threshold (Supplementary Fig. S4). This cell-type-specific difference can be understood from the metabolic context. In normoxic cancer cells both glycolysis and the pentose phosphate pathway (PPP) operate at low rates, so the overall impact of AMPK-dependent regulation is limited. In CAFs, by contrast, both pathways are highly active, which markedly increases the sensitivity of the metabolic network to AMPK activity and explains why β_{AMPK} becomes critical for the W phenotype.

Because β_{AMPK} played a minor role in normoxic cancer cells, we next examined the influence of n. Increasing n promoted the RW phenotype even at relatively low values of β_{HIF}, indicating that steeper regulatory responses facilitate the switch (Figure 4A). Based on these analyses, we selected $\beta_{HIF} = 20$, $\beta_{AMPK} = 20$, and $n = 3$ for all subsequent simulations.

Oxygen availability.

We next examined how the oxygen tension of individual cells determines the outcome of fibroblast reprogramming. The steady-state oxygen concentration was varied independently in the hypoxic cancer cell and in the fibroblast. The resulting phenotypic map (Figure 4B) shows that fibroblast switching is restricted to a defined oxygen window. The cancer cell must first transition to the W phenotype, which occurs when its oxygen level falls below approximately 36.5 μM. Once this condition is met, the fibroblast undergoes ROS-mediated reprogramming only if its

own oxygen tension lies between 33.0 and 45.3 μM. At higher oxygen levels the fibroblast retains the O phenotype. At very low oxygen it switches to W autonomously due to hypoxia itself, and this switch cannot be attributed to ROS-mediated signaling. Within the permissive range, lower oxygen concentrations accelerate the transition. These results imply that fibroblasts must already be in a mildly compromised environment for the ROS signal to become effective. The signal does not force a switch from a fully stable oxidative state but rather directs cells that are already near a regulatory threshold.

Switching in the fibroblast is often preceded by a period of lactate uptake by the cell itself [45]. Our model reproduces this behavior: the fibroblast in the three-cell configuration takes up lactate before switching to the W phenotype (Supplementary Fig. S5). However, this reprogramming requires the hypoxic cancer cell to transition to the W state. If the duration of hypoxia is insufficient and the cancer cell remains in a hybrid W/O state, then the fibroblast does not undergo a phenotypic transition. In this scenario, both the fibroblast and the normoxic cancer cell continue to take up lactate (Figure 4C). Such a discrepancy may reflect either a genuine, as-yet-unreported behavior of fibroblasts or a limitation of the presented model, in which lactate acts primarily as a metabolic substrate and is not treated as a signaling molecule in the regulatory module. Further experimental validation is required to distinguish between these causes.

Glucose availability.

In tumors, the hybrid W/O phenotype is frequently observed [2], and our analysis suggests a metabolic basis for this prevalence. The W/O state is bioenergetically robust under a wide range of conditions and outperforms the pure W and O phenotypes under several stress scenarios. However, under pronounced substrate limitation the RW phenotype becomes superior. To quantify this, we compared the steady-state ATP concentration in RW and W/O cells while systematically varying the extracellular glucose concentration and the lactate degradation rate constant

k_{d_LAC} (Figure 4D). At low glucose, RW cells maintain a higher ATP level than W/O cells. This advantage diminishes when k_{d_LAC} is increased, because rapid extracellular lactate removal reduces the substrate available for RW cells. The relative benefit of RW therefore depends both on glucose scarcity and on the efficiency of lactate clearance from the microenvironment.

Critically, the magnitude of the RW advantage is tightly linked to the supply of extracellular lactate. Lactate can be provided by hypoxic tumor cells, but the most abundant and sustained source is likely to be reprogrammed glycolytic fibroblasts [9]. When fibroblast participation is absent or insufficient, the total extracellular lactate pool remains limited, and RW cells cannot fully realize their bioenergetic potential. Overall, W/O uses glucose more efficiently, whereas RW is less dependent on glucose and can sustain ATP production when glucose is scarce, provided that lactate remains available [46].

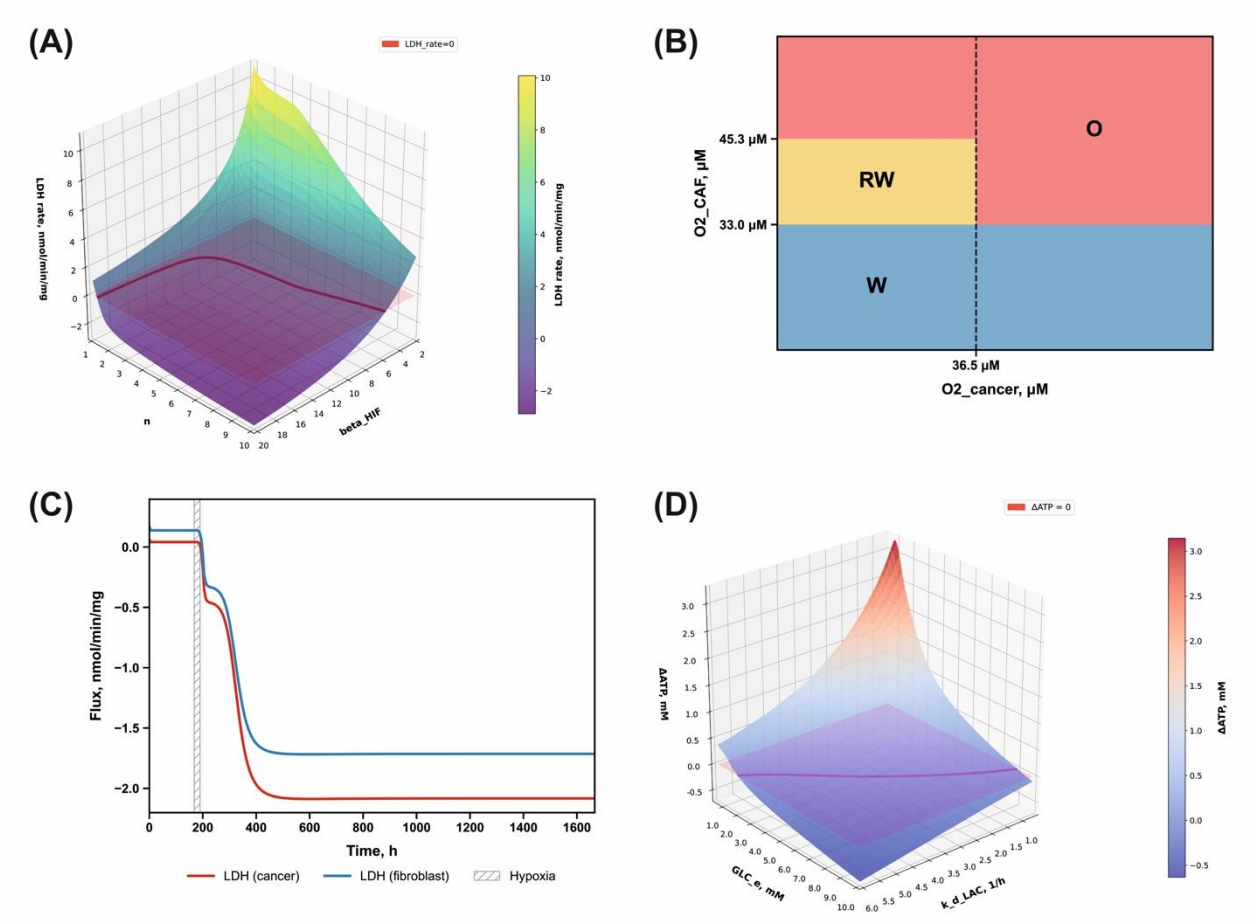


Figure 4. Parametric analysis. *(A) LDH flux in a normoxic cancer cell as a function of β_{HIF} and the Hill coefficient n. Negative flux indicates lactate consumption (RW phenotype). (B) Phenotypic map in the plane of steady-state oxygen concentrations in the cancer cell and in the fibroblast. The map is divided into distinct regions: the O region indicates that the fibroblast does not switch; the W region indicates autonomous switching to the W phenotype, independent of ROS signaling; the RW region indicates ROS-driven switching to the W phenotype. (C) Lactate uptake by the fibroblast and by the normoxic cancer cell when the hypoxic cell is in the W/O state. (D) Difference in steady-state ATP concentration between RW and W/O cells as a function of extracellular glucose and the lactate degradation rate constant k_{d_LAC}. Positive values indicate an energetic advantage of RW over W/O.*

Model limitations and proposed experimental validations

The developed modular framework has several limitations. The regulatory module uses a uniform time delay and identical Hill-type functions for all enzymes, whereas real transcription–translation kinetics and enzyme sensitivities vary considerably. A number of parameters were calibrated manually rather than taken from direct measurements, introducing uncertainty into the quantitative predictions. The model does not also include additional signaling pathways such as PI3K/Akt/mTOR, MYC, or p53. Cell number is limited to three, spatial structure is approximated only through ρ, and heterogeneity within a single cell type is not considered. In addition, detailed kinetic modules for other metabolic pathways — such as the reactions of the Krebs cycle, fatty acid oxidation, and glutamine metabolism — are not included. A more detailed description of these pathways could improve the accuracy of the model's predictions [47] and would constitute a natural next step in its development.

Despite these simplifications, the model makes a number of predictions that can be tested experimentally. It predicts sharp temporal thresholds for the O→W/O and W/O→W transitions, and it defines the oxygen windows within which a cancer cell commits to glycolysis and a fibroblast becomes susceptible to ROS-mediated reprogramming. Confronting the model with experimental data would also require measuring extent to which HIF-1 and AMPK regulate enzyme expression. Under glucose limitation, the RW phenotype is predicted to maintain a higher ATP level than the W/O phenotype, and this difference depends on the availability of extracellular lactate. An important experimental verification would therefore be to identify the boundary conditions under which one phenotype becomes energetically more favorable than the other.

In summary, we have developed a modular framework that integrates cellular metabolism, regulatory signaling, and intercellular communication. By capturing the dynamic interplay between hypoxic and normoxic cancer cells and cancer-associated fibroblasts, the model provides a quantitative basis for understanding the emergence of metabolic heterogeneity and plasticity within tumors.

Data Availability

The modular kinetic model can be accessed and simulated on the BioUML web-server using the Demo mode: https://uni.sirius-web.org:58443/#de=data/Collaboration/Final%20project/Data/Model_1.

All model files, Jupyter Notebooks, and scripts reproducing the simulation results and figures are publicly available in the GitLab repository: https://gitlab.sirius-web.org/AndreyNaumenya/reverse-warburg-effect.

Author Contributions

Conceptualization, A.S.N. and I.R.A.; methodology, I.R.A.; formal analysis and investigation, A.S.N.; writing—original draft preparation, A.S.N.; writing—review

and editing, I.R.A.; supervision, I.R.A. All authors have read and agreed to the published version of the manuscript.

Acknowledgements

We would like to thank Prof. Oleg Demidov and Dr. Alexey Kolodkin for the fruitful discussions and helpful comments.

Funding

This research was supported by the Ministry of Science and Higher Education of the Russian Federation, (Agreement 075-10-2025-017 from 27.02.2025)

References

1. Siegel, R. L., Kratzer, T. B., Wagle, N. S., Sung, H. & Jemal, A. Cancer statistics, 2026. *CA. Cancer J. Clin.* **76**, e70043 (2026).
2. Demicco, M., Liu, X.-Z., Leithner, K. & Fendt, S.-M. Metabolic heterogeneity in cancer. *Nat. Metab.* **6**, 18–38 (2024).
3. Pendleton, K. E., Wang, K. & Echeverria, G. V. Rewiring of mitochondrial metabolism in therapy-resistant cancers: permanent and plastic adaptations. *Front. Cell Dev. Biol.* **11**, 1254313 (2023).
4. Fendt, S.-M., Frezza, C. & Erez, A. Targeting Metabolic Plasticity and Flexibility Dynamics for Cancer Therapy. *Cancer Discov.* **10**, 1797–1807 (2020).
5. Tufail, M., Jiang, C.-H. & Li, N. Altered metabolism in cancer: insights into energy pathways and therapeutic targets. *Mol. Cancer* **23**, 203 (2024).
6. Warburg, O., Wind, F. & Negelein, E. The metabolism of tumors in the body. *J. Gen. Physiol.* **8**, 519–530 (1927).

7. Chen, L. *et al.* Lactate-Lactylation Hands between Metabolic Reprogramming and Immunosuppression. *Int. J. Mol. Sci.* **23**, 11943 (2022).
8. Fu, Y. *et al.* The reverse Warburg effect is likely to be an Achilles' heel of cancer that can be exploited for cancer therapy. *Oncotarget* **8**, 57813–57825 (2017).
9. Pavlides, S. *et al.* The reverse Warburg effect: aerobic glycolysis in cancer associated fibroblasts and the tumor stroma. *Cell Cycle* **8**, 3984–4001 (2009).
10. Guido, C. *et al.* Metabolic reprogramming of cancer-associated fibroblasts by TGF-β drives tumor growth: connecting TGF-β signaling with 'Warburg-like' cancer metabolism and L-lactate production. *Cell Cycle* **11**, 3019–3035 (2012).
11. Martinez-Outschoorn, U. E. *et al.* Oxidative stress in cancer associated fibroblasts drives tumor-stroma co-evolution: A new paradigm for understanding tumor metabolism, the field effect and genomic instability in cancer cells. *Cell Cycle* **9**, 3256–3276 (2010).
12. Hui, S. *et al.* Glucose feeds the TCA cycle via circulating lactate. *Nature* **551**, 115–118 (2017).
13. Salminen, A., Kaarniranta, K. & Kauppinen, A. AMPK and HIF signaling pathways regulate both longevity and cancer growth: the good news and the bad news about survival mechanisms. *Biogerontology* **17**, 655–680 (2016).
14. Keerthana, C. K. *et al.* The role of AMPK in cancer metabolism and its impact on the immunomodulation of the tumor microenvironment. *Front. Immunol.* **14**, 1114582 (2023).

15. Pezzuto, A. & Carico, E. Role of HIF-1 in Cancer Progression: Novel Insights. A Review. *Curr. Mol. Med.* **18**, 343–351 (2018).
16. Smiles, W. J. *et al.* New developments in AMPK and mTORC1 cross-talk. *Essays Biochem.* **68**, 321–336 (2024).
17. Moldogazieva, N. T., Mokhosoev, I. M. & Terentiev, A. A. Metabolic Heterogeneity of Cancer Cells: An Interplay between HIF-1, GLUTs, and AMPK. *Cancers* **12**, 862 (2020).
18. Wallace, D. C. Mitochondria and cancer. *Nat. Rev. Cancer* **12**, 685–698 (2012).
19. Wang, X. & Xiong, X. Mitochondrial Reactive Oxygen Species (mROS) Generation and Cancer: Emerging Nanoparticle Therapeutic Approaches. *Int. J. Nanomedicine* **20**, 6085–6119 (2025).
20. Aghakhani, S., Silva-Saffar, S. E., Soliman, S. & Niarakis, A. Hybrid computational modeling highlights reverse Warburg effect in breast cancer-associated fibroblasts. *Comput. Struct. Biotechnol. J.* **21**, 4196–4206 (2023).
21. Mosca, E. *et al.* Computational modeling of the metabolic States regulated by the kinase akt. *Front. Physiol.* **3**, 418 (2012).
22. Shan, M., Dai, D., Vudem, A., Varner, J. D. & Stroock, A. D. Multi-scale computational study of the Warburg effect, reverse Warburg effect and glutamine addiction in solid tumors. *PLoS Comput. Biol.* **14**, e1006584 (2018).
23. Yu, L. *et al.* Modeling the Genetic Regulation of Cancer Metabolism: Interplay between Glycolysis and Oxidative Phosphorylation. *Cancer Res.* **77**, 1564–1574 (2017).

24. Jia, D. *et al.* Elucidating cancer metabolic plasticity by coupling gene regulation with metabolic pathways. *Proc. Natl. Acad. Sci. U. S. A.* **116**, 3909–3918 (2019).
25. Brown, P. N., Byrne, G. D. & Hindmarsh, A. C. VODE: A Variable-Coefficient ODE Solver. *SIAM J. Sci. Stat. Comput.* **10**, 1038–1051 (1989).
26. Hucka, M. *et al.* The Systems Biology Markup Language (SBML): Language Specification for Level 3 Version 2 Core Release 2. *J. Integr. Bioinforma.* **16**, 20190021 (2019).
27. Kolpakov, F. *et al.* BioUML: an integrated environment for systems biology and collaborative analysis of biomedical data. *Nucleic Acids Res.* **47**, W225–W233 (2019).
28. Le Novère, N. *et al.* The Systems Biology Graphical Notation. *Nat. Biotechnol.* **27**, 735–741 (2009).
29. Akberdin, I. R. *et al.* A Modular Mathematical Model of Exercise-Induced Changes in Metabolism, Signaling, and Gene Expression in Human Skeletal Muscle. *Int. J. Mol. Sci.* **22**, 10353 (2021).
30. Kondrakhin, P. Y., Kachnov, V. A., Akberdin, I. R. & Kolpakov, F. A. A Modular Mathematical Model of Fermentation in an Industrial-Scale Bioreactor. *Processes* **13**, 3288 (2025).
31. Miroshnichenko, M. I., Kolpakov, F. A. & Akberdin, I. R. A Modular Mathematical Model of the Immune Response for Investigating the Pathogenesis of Infectious Diseases. *Viruses* **17**, 589 (2025).

32. Kutumova, E., Kiselev, I., Sharipov, R., Lifshits, G. & Kolpakov, F. Mathematical modeling of antihypertensive therapy. *Front. Physiol.* **13**, 1070115 (2022).
33. Ullah, M. S., Davies, A. J. & Halestrap, A. P. The plasma membrane lactate transporter MCT4, but not MCT1, is up-regulated by hypoxia through a HIF-1alpha-dependent mechanism. *J. Biol. Chem.* **281**, 9030–9037 (2006).
34. Muz, B., de la Puente, P., Azab, F. & Azab, A. K. The role of hypoxia in cancer progression, angiogenesis, metastasis, and resistance to therapy. *Hypoxia* **3**, 83–92 (2015).
35. Halestrap, A. P. The mitochondrial pyruvate carrier. Kinetics and specificity for substrates and inhibitors. *Biochem. J.* **148**, 85–96 (1975).
36. Halestrap, A. P. The monocarboxylate transporter family--Structure and functional characterization. *IUBMB Life* **64**, 1–9 (2012).
37. Zimmer, A. D., Walbrecq, G., Kozar, I., Behrmann, I. & Haan, C. Phosphorylation of the pyruvate dehydrogenase complex precedes HIF-1-mediated effects and pyruvate dehydrogenase kinase 1 upregulation during the first hours of hypoxic treatment in hepatocellular carcinoma cells. *Hypoxia* **4**, 135–145 (2016).
38. Jones, N. M. & Bergeron, M. Hypoxic preconditioning induces changes in HIF-1 target genes in neonatal rat brain. *J. Cereb. Blood Flow Metab. Off. J. Int. Soc. Cereb. Blood Flow Metab.* **21**, 1105–1114 (2001).

39. Samanta, D. & Semenza, G. L. Metabolic adaptation of cancer and immune cells mediated by hypoxia-inducible factors. *Biochim. Biophys. Acta Rev. Cancer* **1870**, 15–22 (2018).

40. Gupta, R. K. & Yushok, W. D. Noninvasive 31P NMR probes of free Mg2+, MgATP, and MgADP in intact Ehrlich ascites tumor cells. *Proc. Natl. Acad. Sci. U. S. A.* **77**, 2487–2491 (1980).

41. Fan, T. *et al.* Tumor Energy Metabolism and Potential of 3-Bromopyruvate as an Inhibitor of Aerobic Glycolysis: Implications in Tumor Treatment. *Cancers* **11**, 317 (2019).

42. Liu, Q., Palmgren, V. A. C., Danen, E. H. & Le Dévédec, S. E. Acute vs. chronic vs. intermittent hypoxia in breast Cancer: a review on its application in in vitro research. *Mol. Biol. Rep.* **49**, 10961–10973 (2022).

43. Hu, X., Chao, M. & Wu, H. Central role of lactate and proton in cancer cell resistance to glucose deprivation and its clinical translation. *Signal Transduct. Target. Ther.* **2**, 16047 (2017).

44. Venning, F. A. *et al.* Deciphering the temporal heterogeneity of cancer-associated fibroblast subpopulations in breast cancer. *J. Exp. Clin. Cancer Res. CR* **40**, 175 (2021).

45. Tan, S., Zhou, F. & Wu, X. Lactate-Mediated Crosstalk Between Tumor Cells and Cancer-Associated Fibroblasts: Mechanisms and Therapeutic Opportunities. *Int. J. Mol. Sci.* **26**, 5583 (2025).

46. Minami, N. *et al.* Lactate Reprograms Energy and Lipid Metabolism in Glucose-Deprived Oxidative Glioma Stem Cells. *Metabolites* **11**, 325 (2021).

47. Villela-Castrejon, J. *et al.* Computational modeling of cancer cell metabolism along the catabolic-anabolic axes. *NPJ Syst. Biol. Appl.* **11**, 46 (2025).

Supplementary Files

This is a list of supplementary files associated with this preprint. Click to download.

- SupplementarymaterialNaumenyaAkberdin.docx